Applied Thermal Engineering 269 (2025) 126023

Contents lists available at ScienceDirect

Applied Thermal Engineering

journal homepage: www.elsevier.com/locate/apthermeng

Research Paper

Experimental study of flow boiling cooling in a novel variable density pin–fin device

Jaume Camarasa [*], Montse Vilarrubí, Manel Ibáñez, Pol Rosell, David Beberide, Jérôme Barrau

Sustainable Energy, Machinery and Buildings (SEMB) Research Group, Universitat de Lleida, Pere de Cabrera s/n, Lleida 25001, Spain

ARTICLE INFO

Keywords:
Flow boiling
Pin-fins
Jet-impingement
Heat transfer
Critical heat flux
Flow visualization

ABSTRACT

Flow boiling is an effective cooling technique for microelectronic systems. However, it presents flow instability issues, most of them associated with critical heat flux situations. In recent years, decreasing variable density microstructured heatsinks have been successfully tested, proving that with a suitable pathway design, the flow boiling instabilities can be mitigated. However, increasing variable density design remains largely unexplored, despite obtaining promising results in single-phase applications. The present work is an experimental study that analyzes the flow boiling performance of a novel increasing density pin–fin array with jet impingement technology. Working with DI water at atmospheric pressure, for an inlet temperature of 75 °C (inlet subcooling of 30 K), 3 flow rates (100–150–200 ml/min) were performed under heat fluxes up to 55 W/cm^2. Focusing on the cooling device design, thermofluidic studies were carried out, supported by high-speed flow visualization. The results demonstrated that this unique cooling device reduces bubble blockage while enhancing bubble breakage and departure. In terms of flow patterns, bubbly, plug, slug and annular flow were observed. The main heat transfer mechanisms detected were single-phase convection, saturated boiling, nucleated boiling and film evaporation. The highest heat transfer coefficient (h_{th}) was obtained for the 200 ml/min test and had a value of 9323 W/°C·m^2. The maximum critical heat flux (CHF) achieved was 58.11 W/cm^2 for the 200 ml/min test. A flow boiling performance evaluation was carried out using the dimensionless Boiling utilization (Bu) number. Compared to existing literature, this novel cooling device emerges as one promising solution.

1. Introduction

In recent decades, colling energy demand has increased disproportionately. Sectors such as data centers, automotive, medical or defense work with a high thermal load, mainly due to the continuous miniaturization of advanced electronics. Consequently, an efficient and scalable cooling solution is necessary.

Single-phase liquid cooling is out of question [1]. However, it presents problems of thermal uniformity. The transition leads to two-phase cooling systems, such as pool boiling [2] and flow boiling [3,4], capable of removing a greater amount of heat. Despite being promising cooling techniques, the instabilities that arise during the boiling process, especially the critical heat flux (CHF), make it difficult to implement it in the market.

Flow boiling research has widely studied different types of surface modification for heat transfer enhancement and instabilities mitigation [5–7]. In fact, microchannel structures have been extensively explored, studying changes in aspects such as cross-section [8–11], channel interconnection [12–14] or liquid supply configuration [15,16], among others. Besides, the introduction of inlet-restrictors [17] and cavitied regions [18,19] have mitigated reversal flow and triggered the onset of nucleate boiling (ONB), respectively. Other heatsink structures such as open microchannels [20], microchannels with pin–fin fences [21], manifold microchannels [22] or vapor venting technology [23] have also been successfully tested. In addition, important research in surface treatments has been performed in recent years, focusing on different types of coatings: same as surface material [24], alloys [25], carbon nano tubes [26] and foams [27]. Furthermore, studies on wettability properties have demonstrated the influence of the interaction between substrate material and working fluid in flow boiling performance [28,29]. Moreover, active control systems have also been tested [30,31], demonstrating their capacity to suppress thermal instabilities.

Micro-pin fin heat exchangers emerged as an alternative to multi-microchannels evaporators for two-phase cooling of high power-density electronics, as they enhance mixing and promote uniform flow distribution across the flow region. Pin-fins are one of the most

---

[*] Corresponding author.
E-mail address: jaume.camarasa@udl.cat (J. Camarasa).

https://doi.org/10.1016/j.applthermaleng.2025.126023
Received 4 December 2024; Received in revised form 7 February 2025; Accepted 19 February 2025

promising flow boiling technologies due to their high heat removal, fluid disturbance effect and their ability to provide extra bubble pathway escape routes, having a direct impact on reducing bubble blockage. Although it has been a very studied technology [32], recently several novel geometries have been developed. Deng et al. [33] presented the open-ring pin-fins, based on a double cut out ring geometry. This design triggered bubble nucleation and enhanced their escape. In parallel, Chien et al. [34] studied in a non-droplet columnar geometry the nucleation core's size effect. Comparing samples of 15 and 45 μm opening width, results showed that the higher pore's shrinkage pore, the lower wall superheat. The reason behind resided in the induction of a higher negative pressure regions in the internal pore, needing less temperature to boil. Furthermore, and inspired by the geometric variability found in nature, Woodcock et al. [35] developed the piranha pin–fin. This design introduced an internal cavity too, in order to boost and provide more stable flow boiling. Tested with the dielectric fluid HFE-7000, this geometry could dissipate more than 700 W/cm^2.

Moreover, Ma et al. [36] analyzed the size and row distribution effects. This work made a comparison where the width and height of the square samples varied from 30 to 50 μm and 60 to 120 μm, respectively. In addition, in-line and staggered row arrangements were studied. Results showed that the staggered distribution enhanced the heat transfer coefficient (HTC) due to their higher flow disturbance effect. In addition, it was concluded that the higher the size, the CHF achievement, caused by an enlargement of the heat transfer area. In parallel, Law and Lee [37] studied the repercussions of the distance between pin-fins. This investigation performed different flow boiling tests on oblique pin–fin arrays with a gap between structures of 0.15, 0.30 and 0.45 mm, respectively. Authors concluded that the larger the distance between pin–fins, the lower HTC was achieved, due to the vapor cluster and consequently local dry-out in the interconnection joints.

However, one of the most interesting pin–fin parameter designs is its density variability. Markal et al. [38] made a comparison between straight microchannels and decreasing variable pin–fin array. This work showed that this novel distribution could enhance the HTC from 371 to 770 %, a part of reducing the wall superheat up to 89.5 %. In addition, the pressure drop could be minimized up to 45.7 %. In comparison with conventional microchannels, this novel design triggered ONB and provided multiple passages to let bubble escape in an easier way. Besides, this pin–fin distribution intensified liquid rewetting and boosted enlarge bubble break up. Furthermore, Markal et al. [39] stated that the expanding density array, compared to a uniform pin–fin distribution, could enhance the HTC by 360 %. The reason behind was that the unfinned zone increased the unforeseen bubble growth between the heatsink outlet and this last region, generating a vacuum effect and, consequently, dragging vapor downstream. In addition, no reversal flow was observed, and lower inlet temperature wall fluctuations were achieved, due to its bubble dynamics improvement. Moreover, Markal et al. [40] compared a uniform array with two different decreasing variable pin–fin density, focusing the flow boiling performance on the gradual density aspect. The unique difference between them was the total downstream regions: 3 and 4, respectively. Despite obtaining better results with decreasing variable density pin–fin arrays, authors stated that a deeper study was needed, with a focus on the relation between downstream cross-sectional area ratio and flow rate, in order to obtain a higher flow boiling yield.

As described, pin–fin variable density designs are promising solutions for two-phase flow. However, only decreasing variable density configurations have been extensively tested. The effect of increasing variable density remains unexplored, despite promising results in single-phase flow [41], as it progressively enhances both the convective heat transfer coefficient and the overall heat exchange surface along the flow path. To address this gap, this experimental study analyzes the flow boiling performance of a pin–fin array prototype, offering basic information for further advancements in boiling applications. Supported by high-speed images, bubble dynamics and flow pattern analysis were discussed. In addition, parameters such as boiling curves, both heat transfer mechanisms and performance, and flow boiling instabilities were assessed. Moreover, a flow boiling performance evaluation was conducted, comparing this novel cooling device with others from the literature that were tested under similar experimental conditions.

2. Experimental design and methodology

2.1. Test bench

Fig. 1 shows the experimental flow loop. It consisted of a primary circuit (where the test module was evaluated) and two secondary circuits (one to heat up and the other to cool down the primary circuit). The chosen working fluid for all of them was deionized (DI) water, due to their high heat removal capacity, elevated vaporization latent heat, no toxicity, low cost and easy disposal.

In the primary circuit, the fluid was stored in a reservoir, opened to the air, and filtered in a 1-μm filter. The fluid circulated through a piping system made of high temperature resistant Teflon, which were insulated by a foam coating. Pumped and adjusted by a diaphragm pump, the flow rate was measured by a Coriolis flowmeter. To reach and maintain the desirable inlet temperature at the test section, a hot secondary circuit was introduced, that consisted of a hot thermostatic bath, a centrifugal pump and a heat exchanger. In addition, a preheater was also used to finally adjust the inlet temperature in a more precise way, thanks to a DC power unit supply and a solid-state relay. After the test module, and before returning to the storage unit, the outlet mixture was cooled down by a cold secondary circuit, with a similar configuration as the hot one.

In addition, the primary circuit was monitored by type-K thermocouples, absolute pressure transducer and differential pressure transducers. The first ones gave thermal values of the most important test bench positions (heating and cooling processes and test module). The second provided the absolute room's pressure. And the last one let authors know the pressure given by the primary pump, the test module's pressure drop and the differential pressure between the test section and the room. All the data was recorded by a data acquisition system. In parallel, flow visualization was performed by a high-speed camera and a lens, supported by a lightning unit.

More details from the experimental set up devices and sensors are shown in Table 1.

2.2. Test module

Fig. 2 shows the test module assembly. It consists of the following parts: platform (1), Bakelite insulation block (2), heater's housing (3), heater (4), thermal paste (5–8), copper block's housing (6), cooper block (7), heat sink (9), silicone sealing gasket (10) and distributor (11). In addition, threaded rods (12), washers (13) and nuts (14) were used to guarantee the correct assembly's fixation and flatness. Furthermore, hydraulic fittings (15) within each Teflon pipe (16) were in the distributor's inlet and outlets.

Jet-impingement technology was chosen as an inlet/outlet arrangement due to its higher heat removal capacity, in comparison with a conventional configuration. So, the fluid entered to the section by an optimized slot [41] located in the centre of the heat sink, below the entry control volume of the distributor. After the flow impacted in the heatsink, it was divided by two parts. Next to crossing the cooling devices, the fluid entered to the outlet volume and finally exited (Fig. 3).

A 100 μm layer of thermal paste (RS PRO 217-3835) was used to seal some parts of the cooling device. It was also in contact with the ceramic heater resistance (same as the preheater; specified in Table 1). In addition, copper and thermal paste conductivity were considered constant, and their values were 398 and 2.9 W/(m·K), respectively.

Distributor, copper blocks and heater's housing were fabricated by a resin printer (Original Prusa SL1S SPEED 3D printer) which had a resolution of ±50 μm. A high-temperature resin (clear-type Siraya Sculpt

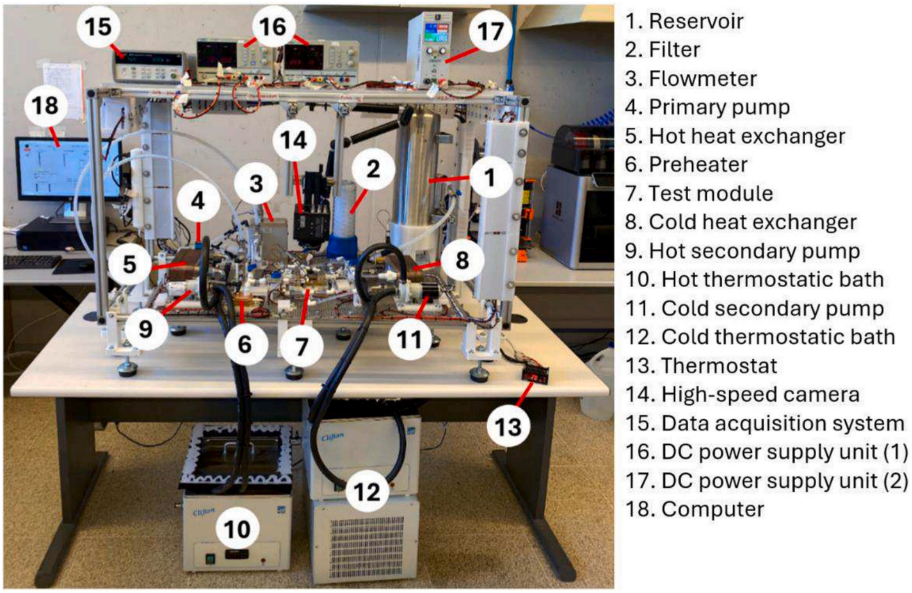

Fig. 1. Experimental test setup.

Table 1
Details of the experimental devices and sensors.

Device	Brand	Model	Specification	Accuracy
Reservoir	Festo	CRVZS-10-G-1	10 l	–
Filter	Aguaplanet	CLC-6295	1 μm	–
Flowmeter	Bronkhorst	M15-AGD-22-0	0–5 l/min	0.2 %
Teflon tubes	Cohiner	1005 T06-00	130 °C at max	–
Primary circuit pump	KNF	Flodos NF-60	0.6 l/min at max 1 bar at max	–
Secondary circuit pumps	Xylem	Flojet DC15/5	23 l/min at max	–
Hot thermostatic bath	Nickel-Electro	NE1D-14	1000 W	0.1 °C
Cooling unit	Nickel-Electro	DC1-300	800 W	0.1 °C
Heat exchangers	Xylem	144–9312	−190 to 232 °C	–
Cooler's temperature probe	RS PRO	124–1082	−60 – 150 °C	0.5 °C
Cooler's temperature controller	RS PRO	124–1047	−60 – 150 °C	0.1 °C
Absolute pressure transducer	Omega	PXM319-002AI	0–2 bars	0.25 %
Differential pressure transducer	Omega	PX26-005DV	0–0.34 bar	0.2 %
Differential pressure transducer	Omega	PX26-015DV	0–1 bar	0.2 %
type K thermocouple	Omega	TJC36-CPSS-020U-6	0–260 °C	0.75 %
High-speed camera	Photron	FASTCAM Mini AX50	50–2000 fps	–
Lens	Navitar	12X	12 mm fine focus	–
Lighting unit	GS Vitec	MultiLED QX	12000 lm	–
Heater and preheater	Watlow Ultramic 600	CER-1-01-00004	0–154 W/cm^2	–
DC power supply unit (1)	METRIX	AX 1360-P	180 W and 6 A	0.1 %
DC power supply unit (2)	Elektro-Automatik	EA-PSI-9500-10 T	1500 W and 10 A	0.1 %
Solid-state relay (preheater)	Carlo Gavazzi	RGC1P23V12EA	10 VDC and 15 A	–
Data acquisition	Keysight	34972A	3 Msps	–
Slot	Keysight	34970A	20 channels	–

Tech) was used because it could perfectly work until 170 °C and provided an excellent transparency for flow visualization. In parallel, the copper layer stored a total of 13 type-K thermocouple that measured the temperature distribution along the flow path. More details about this part and the other components can be found in a previous study [42]. Furthermore, all assembly parts were measured with a micrometre of ±10 μm of uncertainty (RS PRO Metric electronic caliper, model 243-6616).

The heatsink was made of silicon and etched by lithography and Deep Reactive-Ion Etching (DRIE). The cooling device had 10 mm of width, 50 mm of length and a total thickness of 550 μm (Fig. 4). The pin-fins had a diameter of 200 μm and a height of 300 μm. The novelty of this design lied in achieving a uniform wall temperature, despite the temperature of the working fluid increased along the flow path. For this reason, by increasing the number of pin–fin rows in each region, a local convective area rise was attained. Specifically, there were 5 pin–fin regions (R1 to R5 in Fig. 4), where the space between them decreased from 3.2 to 0.37 mm. The number of regions was designed to introduce continuous variations in fluid's velocity and dynamic pressure, primarily to enhance both bubble nucleation and departure. As a novel contribution, the authors explored a greater number of section than those commonly found in the literature, where most studies employ 3 regions. In this work, five regions were selected to achieve a balance between regional flow boiling visualization and thermofluidic changes along the flow path. Additionally, the length and width were optimized to improve flow visualization and minimize edge effects on temperature measurements, respectively [42,43]. In parallel, heatsink's conductivity was considered constant, with a value of 148 W/(m·K). Moreover, it should be marked that the distance between fin's top and distributor bottom surface was 50 μm, to ensure the correct fluid distribution and avoid capillarity issues.

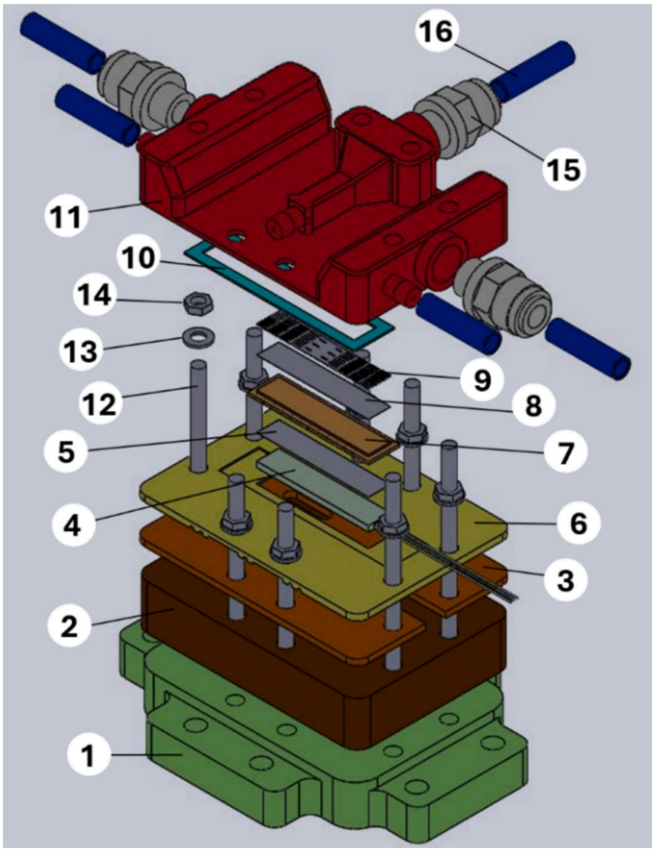

Fig. 2. Exploded view of the test module.

2.3. Operating conditions and experimental procedures

The operating conditions of the experimental study were the following ones: inlet temperature of 75 °C (equal to an approximately 30 K of inlet subcooling), volumetric flow rates of 100, 150 and 200 ml/min (equal to a mass flux of 366.70, 550.06 and 733.41 kg/m^2·s, respectively) and heat fluxes up to 55 W/cm^2. In addition, the working fluid was deionized water at atmospheric conditions.

In parallel, the experimental procedure performed in every test is defined below:

1) Degassing procedure to the working fluid.
2) Flow rate circulation and adjustment.
3) Adjust the hot thermostatic bath to the desirable inlet temperature of the test module.
4) Hot circulating pump and preheater activation to obtain the desirable inlet temperature.
5) If necessary, adjust cold thermostatic bath circuit to achieve a better control of the inlet temperature.
6) Pressure sensors are powered by DC power suppliers.
7) When both flow rate and inlet temperature are stable, AC power is adjusted to reach the desired heat flux. An increment of 2 W/cm^2 is done in both single and two-phase regimes.
8) Once the wall temperature and pressure drop are in steady state, data is recorded at an interval of 1 s for 5 min. Flow visualization is also performed.
9) Steps 7 and 8 repetition until CHF is reached or the highest thermocouple temperature reaches 170 °C (test module damage). At that point, heat flux is turned off at the same time the flow rate is increased to cool down the test module.
10) Each test was repeated 3 times to give scientific validation to the experimentation.

3. Data reduction and uncertainties

3.1. Data analysis

The heat given by the heater (Q_{heater}) is calculated as:

$$Q_{heater} = V \cdot I \tag{1}$$

where V is the voltage and I the intensity given by the power supply unit.

The efficient heat (q_{eff}) absorbed in the cooling device is:

$$q_{eff} = \frac{Q_{heater} - Q_{loss}}{A_b} \tag{2}$$

where Q_{loss} and A_b are the heat losses and heating base area, respectively.

The Q_{loss} parameter was determined by a habitual technique used in the literature [40]. In this method, the test section with no working fluid is subjected to a heat load. For each specified thermal load value, under steady-state conditions, the temperature differential between the mean wall temperature of the heat sink (T_a) and the ambient temperature (T_e) is measured and recorded, represented as $\Delta T_{ae} = T_a - T_e$. Fig. 5 represents the performed heat losses test.

In parallel, A_b is the heating base area, which is the product between

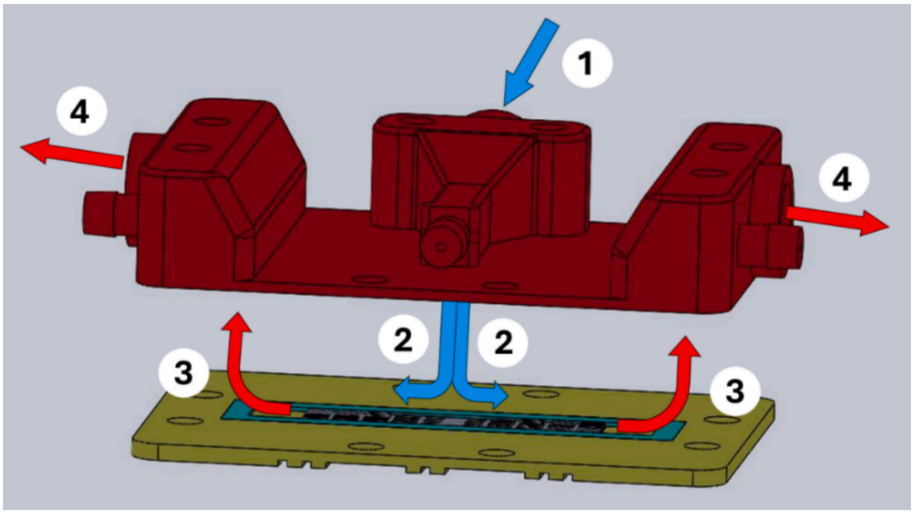

Fig. 3. Sequenced jet-impingement configuration.

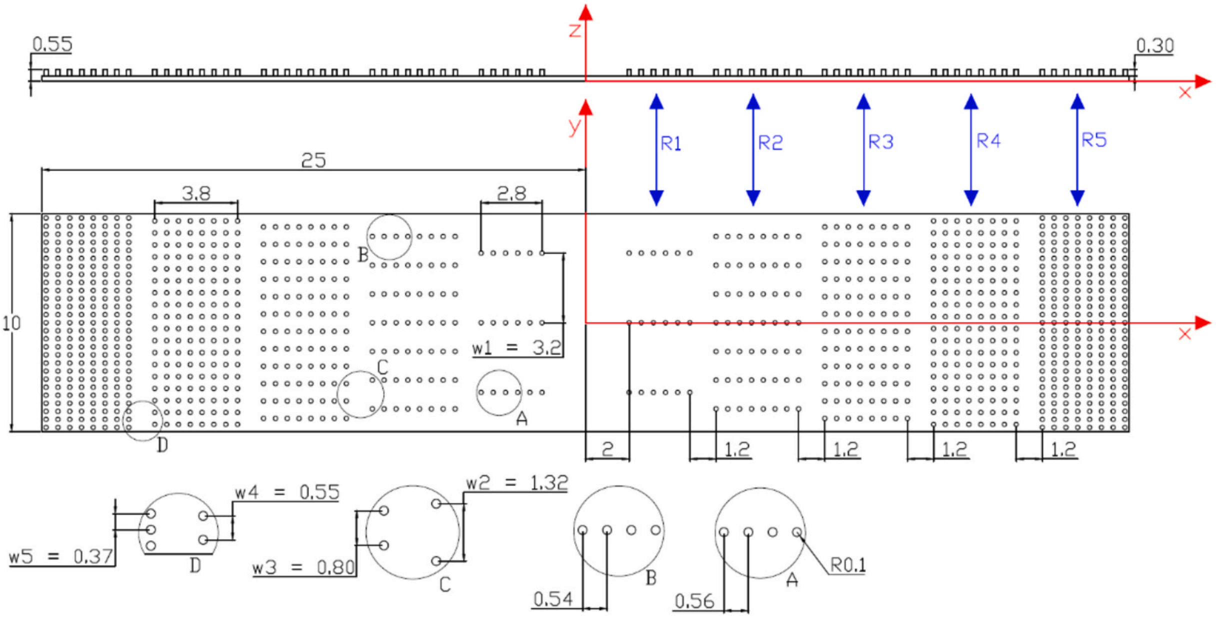

Fig. 4. Heatsink's major dimensions (in mm). In blue, the 5 different regions of the variable density.

the heat sink's length (L) and width (W):

$$A_b = L \cdot W \tag{3}$$

In addition, mass flux (G) can be calculated, too. Due to the fact that the cross-sectional area of each region is different, in order to homogenise the analysis, the section of the inlet distributor slot has been considered, taking into account that a unique distributor has been used for the whole experimentation. So, this parameter can be determined as:

$$G = \frac{\rho \cdot \dot{V}}{w \cdot l} \tag{4}$$

where $\dot{V}$ refers to the flow rate given by the flowmeter, ρ is the working fluid density and w and l are the inlet slot's dimensions of the distributor.

In parallel, from a thermodynamic point of view, the conduction thermal resistance (R_{cond}) between a copper's layers thermocouple and the heatsink's top surface it can be calculated as:

$$R_{cond} = R_{T_{sensor}-copper} + R_{TIM} + R_{Si} = \frac{e_{T_{sensor}-copper}}{k_{Cu}} + \frac{e_{TIM}}{k_{TIM}} + \frac{e_{Si}}{k_{Si}} \tag{5}$$

where the parameter e and k are vertical distance between every component, and the thermal conductivity, respectively.

The wall temperature at specific location ($T_{wall,i}$) is defined as:

$$T_{wall,i} = T_i - q_{eff}'' \cdot R_{cond} \tag{6}$$

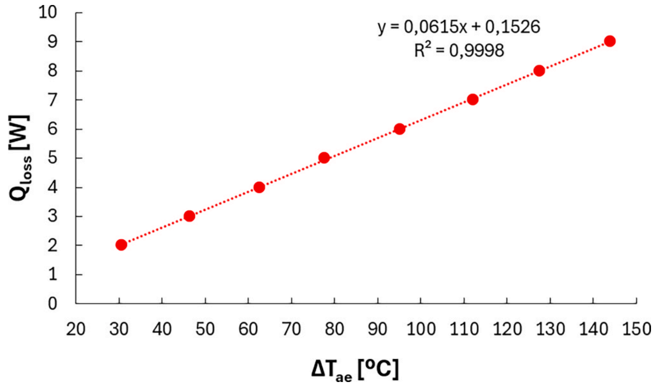

Fig. 5. Heatsink's heat loss equation plot.

where i refers to the position of each thermocouple.

So, the average wall temperature (T_{wall}) can be determined as:

$$T_{wall} = \frac{\sum_{i=1}^{N} T_{wall,i}}{N} \tag{7}$$

where N is the total number of thermocouples measuring in the heatsink.

Furthermore, since saturation temperature (T_{sat}) depend on the working fluid depend, its average absolute pressure and its mass velocity, further research is performed. The specific saturation pressure ($P_{sat,i}$) was calculated as:

$$P_{sat,i} = P_{abs} - \frac{x_i \cdot \Delta P}{L/2} \tag{8}$$

where P_{abs} is the absolute pressure at the distributor's inlet, ΔP is the pressure drop at the test module and x_i is the distance from the test section centreline to the specific thermocouple's location.

Consequently, the average saturation temperature on the heatsink is:

$$T_{sat} = \frac{\sum_{i=1}^{N} T_{sat,i}}{N} \tag{9}$$

Thus, Table 2 provides the saturation temperature for each performed flow rate.

Finally, the total heat transfer coefficient (h_{th}) was determined as:

$$h_{th} = \frac{q_{eff}}{T_{wall} - T_{in}} \tag{10}$$

3.2. Uncertainty of key experimental parameters

Based on the standard method spread in the literature [44], the uncertainty of the key experimental parameters is listed in Table 3.

Table 2
Saturation temperature of every flow rate performed.

Flow rate (ml/min)	Mass flux (kg/m^2·s)	Saturation temperature (°C)
100	366.70	102.13
150	550.06	104.86
200	733.41	104.26

4. Results and discussion

4.1. Bubbly dynamics and flow patterns

High-speed flow boiling visualization is an important tool that helped to identify and understand the different flow patterns and the basic flow events, characterizing and underlying that occurred during the different tests. As a general overview, the different patterns observed in all three tested flow rates were classified as: single-phase regime, bubbly flow, plug flow, slug flow and annular flow (Fig. 6). This classification is intended to be a global characterization of the device that results from the various physical processes that occur in each of the sections and their interactions. It should be remarked that flow visualization was performed in half of the heatsink because due to symmetry conditions the cooling scheme was hydraulically balanced throughout the different experimental tests.

In this design, following the behaviour described in the bibliography [40], most bubbles nucleated just after the pin-fins. In general terms, at initial stages, the nucleated bubbles hadn't enough heat load to grow notoriously, so they were simply created and departed (bubbly flow). As the thermal load increased, a flow regime with more sizeable bubbles started, so bubble coalescence began to be a common phenomenon (plug flow). Therefore, although there were proportionally more small bubbles than large ones, this new scenario exemplified a change in flow pattern. As the heat flux scenario moves forward, the bubble growth rate and its density also incremented. Both processes, being performed closely and simultaneously, raised the continuous appearance of a larger number of big bubbles. So, at this point, this proportion switched, and a flow regime based on big bubbles was consolidated (slug flow). Then, at some stage, distinguished portions of vapor slug were established in the heatsink, surrounded by liquid film, due to the heat flux scenario increase that implied to a fast evaporation of the working fluid (annular flow). Finally, in the final thermal framework, turbulent vapor slug with several dry-out regions was observed in the cooling scheme (CHF situations). Fig. 7 plots the flow pattern distributions for each flow rate.

From Fig. 7, it should be mentioned that all flow patterns were visualized for each flow rate. However, the impact of the thermal load increase was greater in the sample with lower flow rate, causing a faster transition between thermal scenarios. So, in 150 and 200 ml/min tests, the transitions were softer and more predictable, facilitating flow pattern identification. In parallel, authors would like to remark that this characterization plot was an approximate analysis, since in some cases there wasn't a completely uniform and continuous regime (especially in the 100 ml/min test), as can be seen in Fig. 8. Consequently, when analysing the samples in the transient situations, the most observed flow pattern that during the recording was chosen.

In parallel, for future research, it should be remarked that it will be important to consider that a lower flow rate allows to work with different types of regimes in a more immediate way, achieving an increase in energy transfer larger, for a small heat flux increment, than in situations of greater mass flux. So, depending on the range of powers to be dissipated, it seems interesting to evaluate the different scenarios.

From a microscopic point of view, this design provided a unique flow boiling pin–fin distribution that regionally changed the dynamic pressure and fluids velocity, favouring the bubbles nucleation and their movement along the heatsink. It should be remarked that punctually and for certain thermal scenarios, especially at the beginning of each regime, few bubbles get stuck in the heatsink due to surface tensions while most of them leave the heatsink. Bubble coalescence was identified as one of the two main mechanisms (the other one was the notorious increment of the bubble growth rate, compared to bubbly flow) which originated the creation of the plug flow. In parallel, this pin–fin array configuration helped to break up these big bubbles in the final regions (R4 and R5), avoiding bubble blockage.

Table 3
Uncertainty of the calculated parameters.

Calculated parameter	Uncertainty
Q_{in}	0.10 %
Q_{loss}	0.72–1.62 %
q_{eff}	0.11–1.35 %
$\dot{V}$	0.20 %
T_{wall}	3.15–4.72 %
h_{th}	4.80–6.15 %

Condensation and bubble collapse were punctually observed in the 100 and 200 ml/min tests (Fig. 9). These phenomena occurred for both tests in slug flow regime (20.73 and 38.64 W/cm^2, respectively), when big bubbles grew but didn't reach the necessary hydraulic energy to flow across the heatsink. At first sight, in terms of kinematics, bubble formation's growth rate was higher than fluid's velocity. Furthermore, internal forces were induced by the interaction between evaporation momentum force and mixture's surface tensions during bubble coalescence. Consequently, during certain moments, bubbles located in the middle of the heatsink's behalf were stuck in the heatsink, continuously growing. Since plug regime was the main flow pattern, several bubbles were being created at the same time, in the same region and under the same conditions.

Consequently, bubble coalescence led to radial and axial growth, particularly in R3 and R4, where greater spacing between microstructures provided more room for expansion. As the bubble entered the bypass zone—marking the transition between regions—changes in dynamic pressure and velocity became significant. At this point, the local dynamic pressure exceeded that of the pin–fin zone, and the resulting hydraulic forces facilitated the bubble's movement, driving it forward slowly but effectively. So, bubbles collapsed due to condensation when entered to the next downstream region where there was a lower temperature. From a heat transfer perspective, this collapse increased the fluid temperature, ultimately reducing heat extraction efficiency.

In parallel, upstream compressible volume instability (UCVI), and their consequent reversal flow, were visualized in annular flow regimes. This phenomenon usually started in the most microstructured region of the heatsink (R5), either in its centre or in the sidewalls. Due to the rapid growth rate, bubble expansion overcame the hydraulic force and occupied almost half of the heatsink (Fig. 10). This instability induced a reversal flow that caused an increase in the fluid's temperature and, consequently, deteriorated the heat extraction. It should be remarked that this instability was partially and completely observed during the different tests: firstly was detected in R5 and then, as the heat flux increased, was also observed in R4 and R3. The completely UCVI was observed in the last's stages of the annular flow, before originating the boiling crisis. The uncontrolled bubble extension had so much superior growth rate that, helped by the high heat flux scenario, exceeds the hydraulic force and practically occupied the entire heatsink. The partial UCVI was intermittently identified, in R4 and R5, at the beginning of the final stages of annular flow (for all three tests) and, in addition, in the transition between plug and annular flow. Compared to the completely one, this last occurred due to a not enough bubble growth rate that, combined to the disturbance effect between this transition, couldn't be able to hinder the entire occupation of the heatsink.

- This vapor slug remained in the heatsink it due to the intermittent explosive nucleation boiling located in the sidewalls of heatsink, where the mixture was unstable. However, if this nucleation does not occur in either of the two lateral parts of the heat sink, the gas mass detaches from the lateral rows and the cooling fluid gradually manages to overcome the resistance coming from the gas volume, resulting in a general refilling (Fig. 11). It should be remarked that both processes (UCVI and refilling) periodically occurred during the transitional (200 ml/min test) and final stages (for all tests) of annular flow.

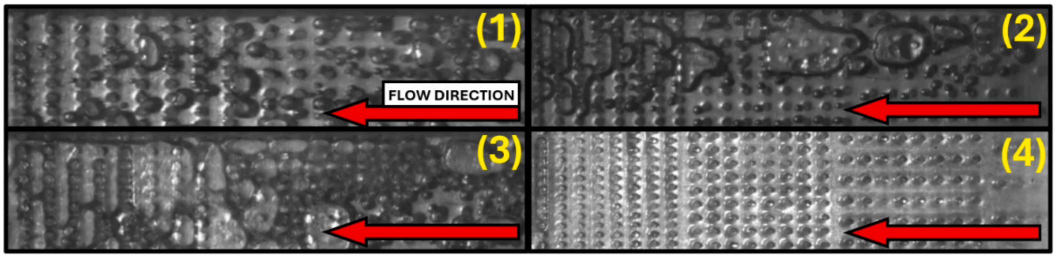

Fig. 6. Flow boiling regimes (1) bubbly flow (2) plug flow (3) slug flow (4) annular flow.

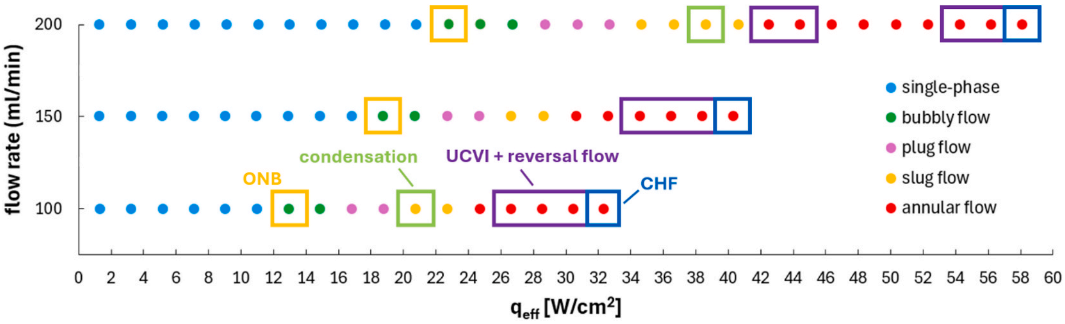

Fig. 7. Bubble dynamics and flow patterns characterization plot.

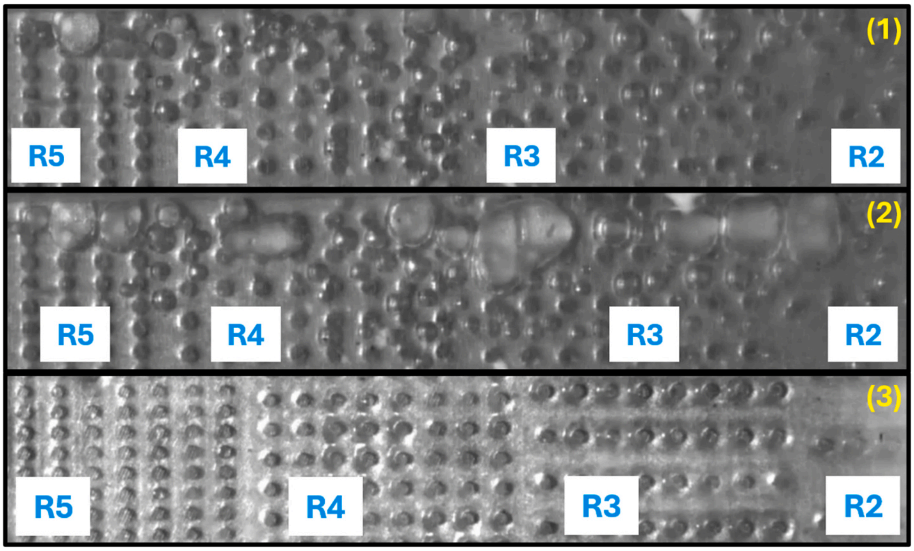

Fig. 8. Regional bubble dynamics (1) 100 ml/min test under 14.87 W/cm^2 (2) 200 ml/min test under 32.71 W/cm^2 (3) 200 ml/min test under 48.37 W/cm^2.

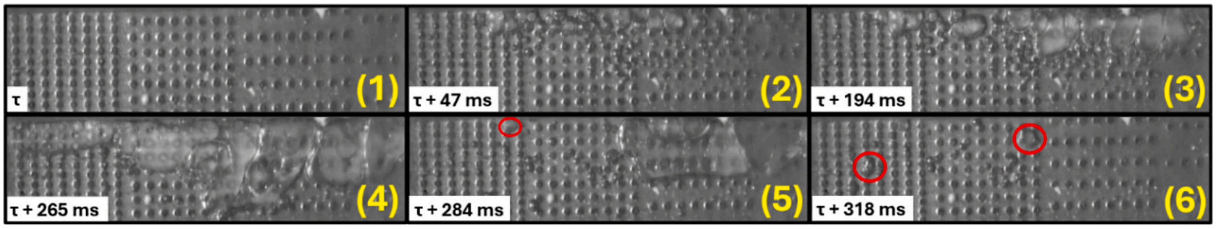

Fig. 9. Condensation phenomenon stages.

4.2. Boiling curves

A clear way to assess the flow boiling thermal performance of the different tests is to plot the boiling curves, that graphically represent the relationship between the wall superheat and the efficient heat (Fig. 12). For a heat flux scenario, the lower the wall superheat, the higher the heat removal performance. Since the inlet temperature was 30 K subcooled with respect to the saturation temperature, two main tendency

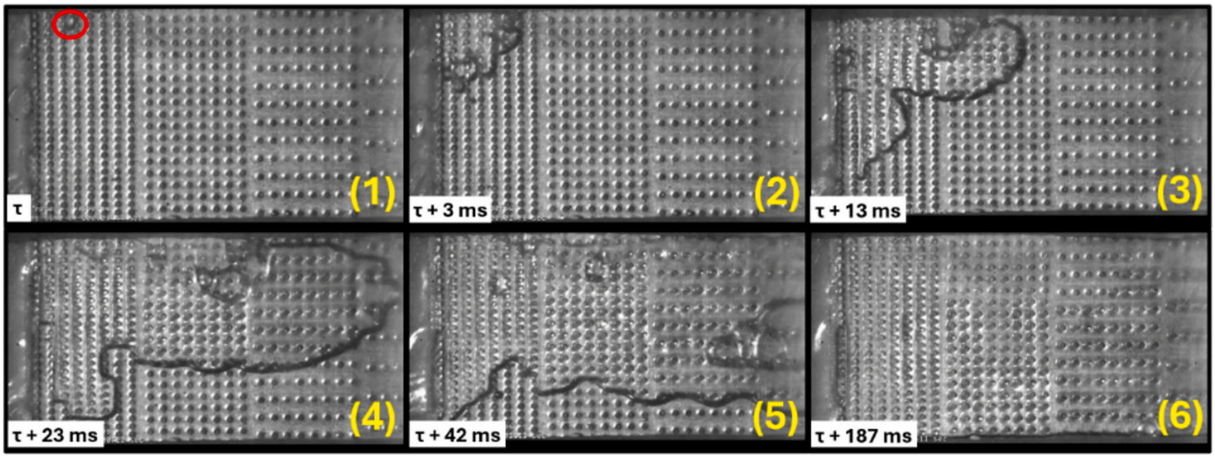

Fig. 10. Steps of the UCVI phenomenon.

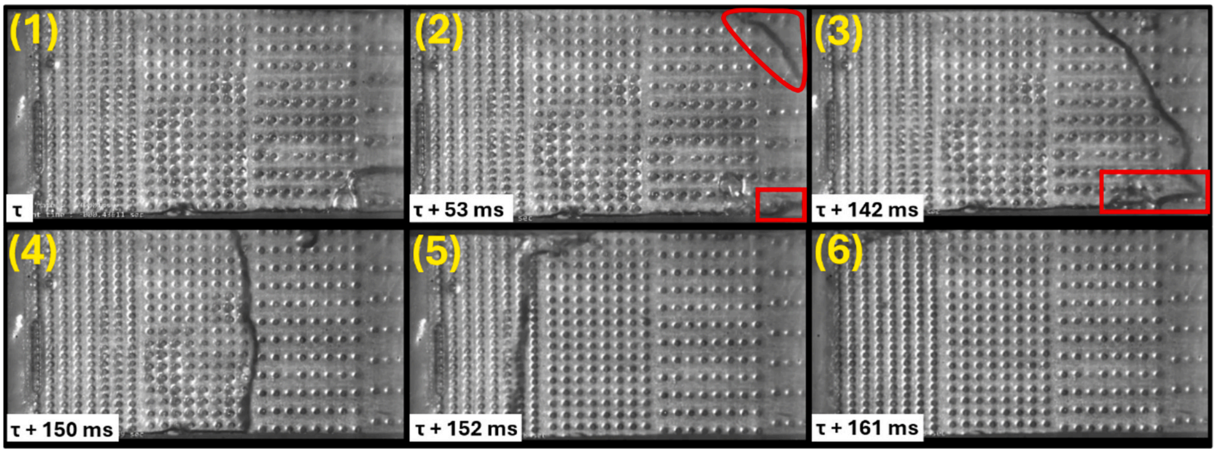

Fig. 11. Stages of the refilling process.

thermal yields were identified: single and two-phase behavior.

As can be observed in Fig. 12 100 ml/min test had a different behaviour from the 150 and 200 ml/min. The reason behind this success relied on that in low flow rates, the change in slope between single and two-phase cooling was barely notorious due to the jet-impingement configuration, a cooling technique that, in comparison with a conventional inlet/outlet arrangement, intrinsically enhances heat removal in region R1. Added to this fact is that the fluid in the annular regime is not capable of consolidating under a large number of thermal loads (consequently, without taking advantage of their best flow boiling performance), the plot obtained at 100 ml/min don't show a high slope [45].

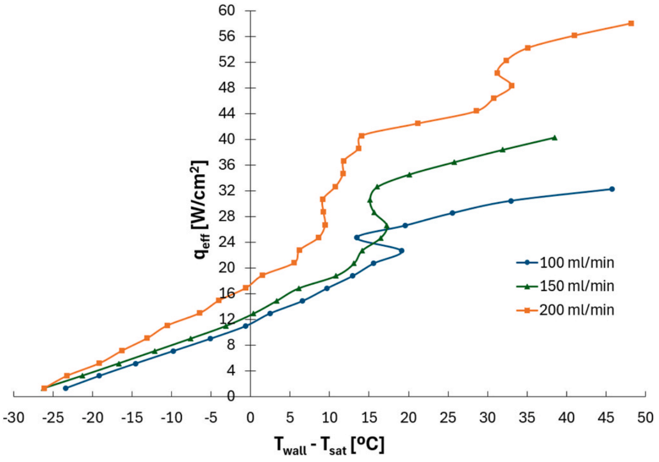

Fig. 12. Boiling curves of the micro-pin–fin heatsink under various flowrates.

Single-phase stage. Each of three tests show an almost constant slope until saturation, demonstrating a constant thermal resistance across the heat flux scenario. The o*nset nucleation boiling* (ONB) phenomenon is identified for an efficient heat flux of 12.93, 18.76 and 22.81 W/cm^2 for the 100, 150 and 200 ml/min tests, respectively.

Two-phase stage. When the two-phase regime was established and the bubbles occupy most of the heatsink, the change in the boiling curves was noticeable. The different wall superheat values when ONB occurred were 2.46, 3.29 and 6.20 °C for 100, 150 and 200 ml/min tests. It should be remarked that this phenomenon was delayed due to the fact that the hydraulic force given by the impact of the working fluid it didn't allow a stable, uniform and continuous nucleation in the first stages just after entering in the saturation zone. This situation was accentuated as the flow rate increased, since the hydraulic force was greater. At the same time, one of the areas that attract the most attention is just after the ONB of the 100 and 150 ml/min tests. These were points that, even if saturated boiling was detected, were still in the transition zone (especially the 100 ml/min test). Therefore, until the bubbly flow regime was established, nucleation was neither uniform nor continuous. Consequently, the linearity of the curves was not as expected.

In parallel, high-speed flow visualization showed that, at initial stages, R3, R4 and R5 were the most suitable regions to achieve a uniform and continuous bubble nucleation. Then, as the thermal load increased, stable flow boiling was consolidated in R2. Bubble departure could be boosted thanks to the regional design. This novel design promoted continuous changes in coolants velocity and dynamic pressure. In fact, the fluid's velocity increases more and more, being counteracted by a constant decrease in its dynamic pressure. Related with this success, it can be noted that as the fluid progresses through the heat sink, where microstructure density is higher, an increase in pressure drop will result in a greater number of bubble nucleation events. Consequently, the two-phase regime had the best scenario as possible: the bubble nucleates, grows and moves away at high frequency, without significant bubble blockage.

Saturated boiling was observed in all of the three tests. In this situation, dispersed bubbly flow was identified, and most of the bubbles were sporadically nucleated from the lasts regions of the heatsink. In parallel, stable nucleating boiling was recognized during plug and slug flow, where the nucleation became periodically uniform in the heatsink. From bubbly to slug flow, the two-phase regime kept constants for all the three tests. However, for the 200 ml/min test, in the initial stages of the annular flow, for an efficient heat flux of situations of 42.53 and 44.45 W/cm^2, turbulent UCVI and reversal flow situation occurred, raising the temperature in the heatsink. However, when the annular flow was stablished, a more vertical shape was obtained.

In addition, hysteresis was observed in all of the tests. This phenomenon occurs when annular flow was fully stablished in the heatsink. When this success happens, film evaporation occurs, enhancing the heat transfer and, consequently, abruptly decreasing the heatsinks wall temperature. Despite some literature related this phenomenon to the high subcooling degree [46], authors consider that in this configuration the subcooling effect did a smaller impact than the flow regime establishment, due to the change of the heat transfer mechanisms during flow pattern transitions.

It should be remarked that no bubble confinement was detected. In fact, the regions with the highest pin–fin density, R4 and R5, broke up major bubbles suppressing bubble blockage. In addition, tip clearance had a considerable effect on avoiding this phenomenon [47]. Consequently, the CHF situations (32.31, 40.31 and 58.11 W/cm^2, respectively) came from the local dry-out developed in the last stages of each test that increased and spread disproportionally, couldn't be successfully rewetted. This instability started for every test when, during annular flow, both UCVI and reversal flow occurred: first partially and then completely, ending up occupying practically the entire device. In the lasts regions of the heatsink, where the vapor core remained almost the whole time during these instabilities, dry-out regions appeared due to the sudden, fast and completely evaporation of the working fluid: firstly located non-uniformly and then globally scattered. Initially, these dry-out regions were continuously rewetted by a liquid film supply thank to capillary forces induced by the pin–fin array, a part of the continuous general refilling. However, as the heat flux increased and the instabilities were more turbulent and unstable, neither the rewetting or the partial refilling weren't enough to cool it down and heatsink's temperature raised (Fig. 13).

As previously stated, in every scenario of advanced annular flow, sporadic and disperses dryness situations occurred in the last regions of the heatsink. Fig. 13 clearly shows the rapid phenomena of local dry-out rewetting. In less than 50 ms, a regional rewetting cycle was completed. As can be appreciated, the liquid film encircled the micro-structures and the mixture flowed between them. It should be remarked that wetted area keeps almost constant due to the molecular interactions between the pin-fins and the fluid. In fact, in this stage, boiling areas were reduced to the multiple internal passages between the fins. Consequently, with an approximately 13 ms since the initial study stage, the firsts rows of the region were rewetted (marked in red) induced by mainly capillary forces, although the extra drag force provided by the explosive nucleate boiling have an impact to be considered. In addition, after 44 ms, a complete rewetting was obtained in almost the whole second half of the region, by surrounding the pin-fins with a liquid film again (marked in blue), thanks to the drag forces provided by the increasing pin–fin cooling scheme design.

4.3. Heat transfer

The variation of the two-phase heat transfer performance is drawn in Fig. 14.

In general, the 100 and 150 ml/min tests exhibited similar behavior, whith heat transfer increasing as heat flux increased, reaching a maximum value when annular flow was established. The subsequent decline in the heat transfer coefficient is attributed to the formation of UCVI and flow reversal, leading to CHF. The 200 ml/min test followed a similar trend until the transition between slug and annular flow occurred. However, after this transition, although the prototype reached a stable heat transfer value in annular flow, it remained lower than the

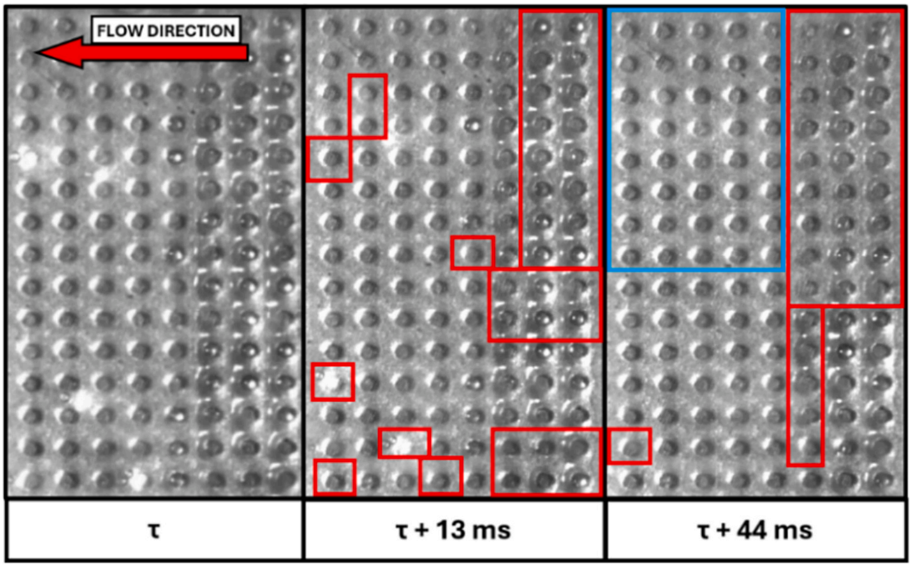

Fig. 13. Local dry-out situations successfully controlled by capillary rewetting in the region 4 of the heatsink. Marked in red, local rewetting. Marked in blue, regional rewetting.

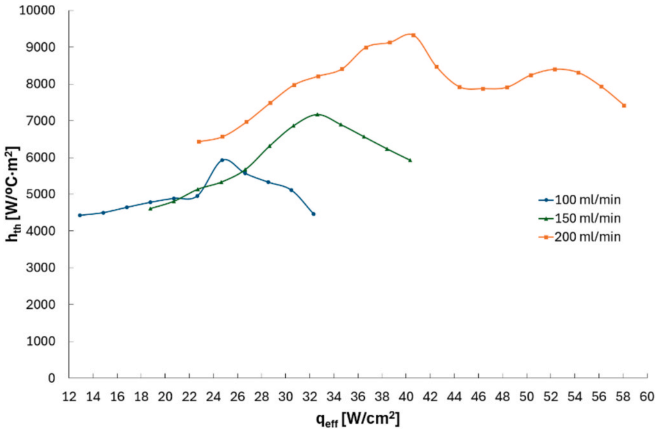

Fig. 14. Heat transfer coefficient curves under various flowrates in two-phase regions.

maximum achieved in slug flow. This reduction is attributed to sustained flow instability, which impeded the establishment of an efficient annular flow regime.

Furthermore, as can be observed in Fig. 14 and related to Fig. 7, the heat transfer mechanism had a strong influence from both flow rate and flow boiling regimes. Dispersed bubbly flow was under saturated boiling. As the bubbly flow became continuous and uniform across the heatsink, nucleating boiling tended to consolidate. In fact, this heat transfer mechanism was fully established during plug and slug flow. Finally, in the course of annular flow, convective film boiling was observed (Fig. 13). In parallel, Fig. 15 was proposed in order to characterize, for every test, the heat transfer mechanism throughout the whole heat flux scenario.

From a macroscopic point of view, similar trends can be observed in Fig. 15. However, a detailed analysis of Figs. 12 and 14, supported by high-speed flow visualization, reveals several key findings. After the ONB, single-phase convection was progressively reduced across the heatsink until consolidating along the centerline, where up to near CHF situations regional film evaporation appeared. This effect was particularly evident at the highest flow rate, where the peak hydraulic force suppressed flow boiling formation. Saturated boiling was observed only during the ONB phenomena across all three tests. As the thermal load was increased, nucleate boiling emerged on the weaker side of the pin-fins [48] located in R3, R4 and R5. Additionally, at higher flow rates, nucleate boiling was enhanced due to bubble departure, driven by the rise in fluid velocity within the most populated regions. Finally, film evaporation exhibited significant differences in the 200 ml/min test, where flow instabilities—associated with upstream compressible vortex interaction (UCVI), flow reversal, and local dry-out (predominantly in R5)—disrupted optimal flow regime performance.

However, several boiling phenomena deteriorated the different heat transfer mechanisms. As described before, condensation and bubble collapse were occasionally detected in consolidated nucleate boiling for the 100 and 200 ml/min tests for a heat flux scenario of 20.73 and 38.64 W/cm^2, respectively. Due to the fact that this phenomenon was intermittently identified during the test, the impact on the heat transfer coefficient was slightly noticeable. Graphically, situated in an increasing trend, it was plotted as a horizontal behaviour, breaking the tendency line. Furthermore, UCVI and reversal flow were the main mechanisms to perform a film evaporation deterioration (mainly in R3, R4 and R5). Since the fluid stayed more time in the heatsink than in ordinary scenario and considering that was an intensification of the heat flux, the convection exchange was poorer. In high heat fluxes scenarios, where theses instabilities shared the stage with non-rewetted local dry-out regions (with specific focus in R4 and R5), ended up deriving in CHF situations.

Moreover, from a quantitative point of view, the maximums heat transfer values achieved in all three tests were 5929, 7173 and 9323 W/°C·m^2, respectively. So, compared to the first stages of bubbly flow of each test, where the mean values were approximately 4426, 4348 and 6173 W/°C·m^2 during saturated boiling, the enhancement achieved was a 33.96, 64.95 and a 51.02 %, respectively. The reason behind the difference of the performances between the 150 and 200 ml/min relies on the scenario full of instabilities in fully developed film evaporation, disabling a higher performance in annular flow.

4.4. *Flow boiling instabilities*

Due to the bubble nucleation phenomena, flow boiling technology intrinsically works in a fluctuate way. Consequently, parameters as pressure drop have an oscillatory behaviour during two-phase cooling. In this section, the transient behaviour was investigated to analyse the temporary bubble dynamics and their impact on the overall pressure drop across the heatsink.

The pressure standard deviation ($\sigma_{\Delta P}$) can be calculated as:

$$\sigma_{\Delta P} = \sqrt{\frac{\sum_{i=1}^{N}\left(\Delta P_i - \overline{\Delta P}\right)^2}{N}} \tag{11}$$

Figs. 16, 17 and 18 represent the transient behaviour of the pressure drop of each test under a heater's heat flux of 24 W/cm^2, 28 W/cm^2 and 34 W/cm^2. The first scenario corresponds to the beginning of the bubbly flow of the 200 ml/min test. The second matches with different flow regimes in every test: annular flow (100 ml/min), slug flow (150 ml/min) and plug flow (200 ml/min). And the third blends with the CHF of the 100 ml/min test and the peak value of heat transfer coefficient of the 150 ml/min test.

As can be clearly observed in all figures, the transient pressure drop behaviour depends on the flow regime and its thermal scenario. In Fig. 16, the beginning of the saturated boiling in the 200 ml/min didn't increase the oscillatory behaviour, due to the fast bubble departure induced by the hydraulic force in this stage in most of the heatsink (end of R2 to R5). In contrast, the consolidated nucleate boiling and film evaporation of the 100 and 150 ml/min, respectively, distinctly show a higher fluctuation. The reason behind this phenomenon relied on the bubble coalescence from R3 to R5, its movement and their consequence

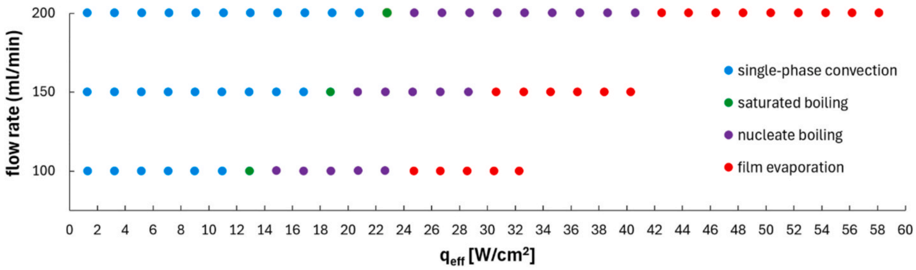

Fig. 15. Heat transfer characterization for the whole thermal scenario.

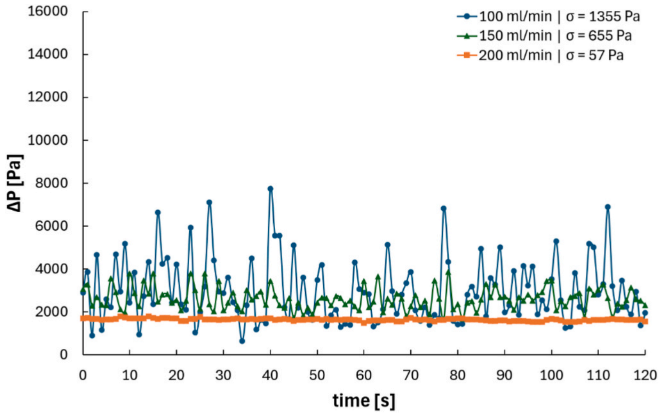

Fig. 16. Transient pressure drop behaviour of each test under a heater's heat flux of 22 W/cm^2.

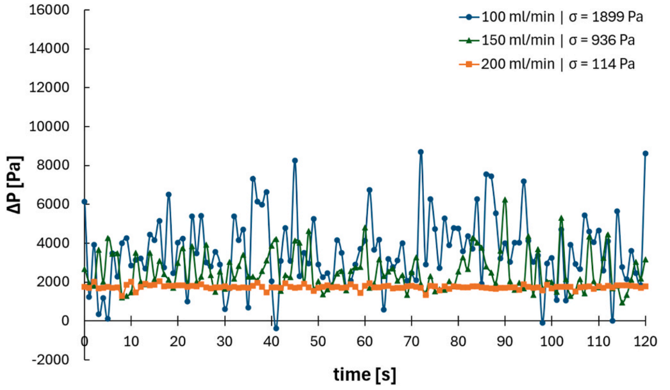

Fig. 17. Transient pressure drop behaviour of each test under a heater's heat flux of 28 W/cm^2.

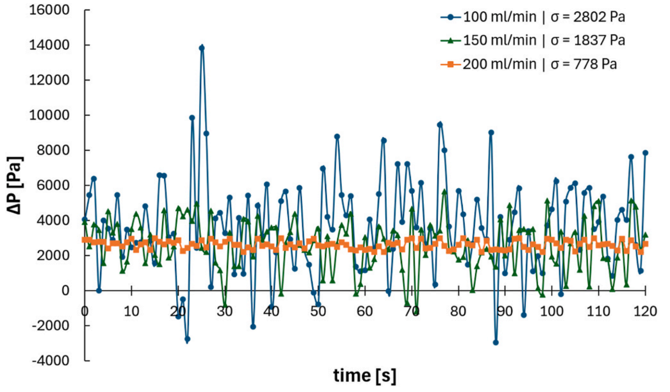

Fig. 18. Transient pressure drop behaviour of each test under a heater's heat flux of 34 W/cm^2.

disturbance effect, that increased the pressure drop fluctuation. Another reason for the more accentuated vibratory behaviour in the 100 ml/min test was the condensation phenomena during nucleate boiling, that intensified mixture disturbance.

In parallel, Fig. 17 shows an increase of pressure drop and a fluctuation intensification of the 100 ml/min test, that worked under film evaporation. In this situation, intermittent UCVI and reversal flow in R5 induced a higher agitation of the flow boiling mixture, also contributed by the general refilling phenomenon. In parallel, the 150 ml/min test raised their oscillatory behaviour too, working under the first stages of slug flow on that thermal scenario. Furthermore, a slightly vibrating behaviour was distinguished in the 200 ml/min test, due to the establishment of the bubbly flow (which was the beginning of the fully consolidation of the nucleate boiling).

In addition, Fig. 18 exemplifies the behaviour observed in the 100 ml/min test under boiling crisis situations. Substantial increase of wall temperature and pressure drop, and the oscillatory nature of this parameter intensified. The reason behind this behaviour lied in the thermofluidic chaos that occurred in CHF situations, where the general refilling was no longer complete, the UCVI phenomenon intensified in multiple locations (most of them in R4 and R5, perhaps some observed in R3) and film evaporation performance decreased notably. Besides, the 150 ml/min test also showed an important increase in its pressure drop behaviour. It should be remarked that this test was working under fully developed film evaporation in most of the heatsink, performing at its best in terms of heat removal. Consequently, a continuous film boiling and rewetting phenomena were operating in a continuous but alternate way. Furthermore, a noticeable oscillatory behaviour was detected in 200 ml/min, corresponding to the consolidation of the plug flow and their bubble dynamics intensification effect (uniform and continuous nucleate boiling in almost the whole heatsink).

From a quantitative point of view, focusing on the standard deviation of every test, its being reaffirmed that a higher mass flux considerably reduces the oscillatory behaviour of the heatsink. Despite enhancing heat removal and mitigating the flow boiling instabilities, a flow rate increases mean an increment in the power consumption. Consequently, a trade-off between future energy savings and chip's safety should be performed.

In addition, it should be remarked that the test module design includes a 50 μm bypass. This gap between the pin-fins top and distributor provided an extra passage for bubbles formation, that certainly helped to avoid bubble blockage situations and enhance flow boiling stability. Consequently, authors consider than, in parallel with literature [49], a better flow boiling behaviour and higher heat removal performance was obtained thanks to the open heatsinks' structure design, especially in thermal scenarios of advanced nucleate boiling and film evaporation, where large layers of gas continuously occupied the cooling device.

Moreover, inspired by the bibliography [50], a flow boiling instability map was plotted in order to clarify the stable regions where the heatsink, under the specific described operating conditions, performed predictably and safely (Fig. 19). However, in this case, the chosen criterium varied. Unstable region was defined as an area where decontrolled UCVI was detected, due to the fact that this instability couldn't be mitigated with the current operating conditions.

Fig. 19 clearly shows a linear relationship between the efficient heat flux, the flow rate and the different tests. This result would be an important criterion for future analysis, when novel heatsinks operating parameter as flow rate, inlet subcooling, working fluid or bypass, among others, need to be evaluated.

4.5. Flow boiling performance evaluation

According to literature [51,52], an evaluation of the flow boiling performance could be obtained by a dimensionless number called Boiling utilization (Bu). This parameter represents the quotient between the heat flux dissipated in the two-phase and single-phase regimes, where thermofluidic successes as ONB heat flux and CHF intervene. Consequently, the higher the value, the better flow boiling performance of the cooling device under specific experimental conditions.

$$Bu = \frac{q_{CHF} - q_{ONB}}{q_{ONB}} \tag{12}$$

An innovative Bu map was presented in this section, where a comparison between different geometries found in the literature was performed. With the main objective to be the most accurate as possible, were only chosen the works which were performed under similar

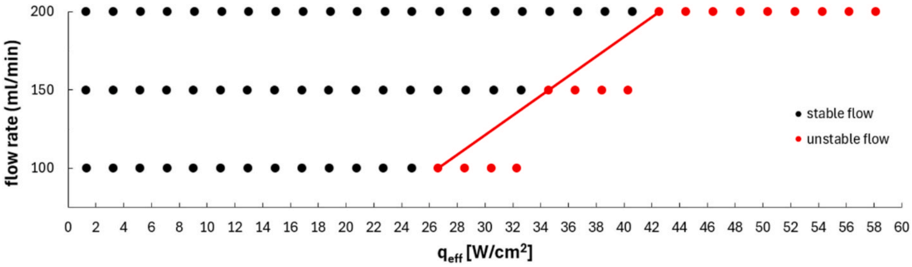

Fig. 19. Flow boiling instability map.

experimental conditions as the ones of this study. These are the following:

- DI water as a working fluid.
- Inlet subcooling of around 35 K.
- Mass flux around 350 kg/m^2·s.

It should be stated that the reason behind choosing a mass flux around 350 kg/m^2·s was that there were more studies that could fit in the comparison.

After a deep revision on the literature, different geometrical heat-sinks could be selected. Microchannels with inclined bottom grooves [53], leaf vein inspired three-tiered open microchannels [54], rhombus pin–fin array [55], microchannels with inlet restrictors [51], counter flow diverging microchannels [56] and ohm-shape microchannels [57] could be evaluated and compared (Fig. 20).

As observed in Fig. 20, despite being inspired by a single-phase design and not optimized for flow boiling conditions, the current heat-sink has a Bu value of 1.50, which is higher than that of most geometries included in the Bu map. Only ohm-shape microchannels (slightly) and counter flow diverging microchannels (notably), which were specifically designed and optimized for flow boiling conditions, achieved better results. In comparison with a uniform pin–fin array, which almost have an identical mass flux, the Bu parameter was 3 times higher in the variable density pin–fin array. In addition, authors would like to remark than, in parallel as described in Camarasa et al. [7], the combination of two or more technologies boosted achieving better results.

For future work, the same major microstructure dimensions should be tested under identical experimental conditions to draw more definitive conclusions. The authors believe that this dimensionless parameter could serve as a valuable tool for an initial flow boiling comparison in further research.

5. Conclusions

The present study provides a novel investigation of an innovative increasing density pin-finned surface, which was experimentally tested under flow boiling conditions. Specifically, this cooling device combines jet impingement entrance and increasing pin–fin distribution. Two-phase experiments were carried out using deionized water at atmospheric conditions, working at 3 different flow rates (100, 150 and 200 ml/min) and an inlet subcooling of approximately 30 K. The heat transfer and flow pattern characteristics were analysed. UCVI and pressure oscillations were also studied. The main conclusions are summarized below:

- This unique design provided several changes in fluid's dynamic pressure and velocity reducing bubble blockage. In parallel, jet-impingement technology promoted heat removal in initial stages. Consequently, the authors consider that implementing both technologies enhanced the flow boiling performance.
- Single-phase, bubbly, plug, slug and annular flow were the main flow patterns identified during the experimental tests. Flow rate has a direct impact on bubble dynamics and flow patterns. Indeed, the lower the flow rate, the faster transitions between flow boiling regimes. Consequently, it needs to be considered for future applications.
- Showing slope changes during the boiling curves, different heat transfer mechanisms were recognized: single-phase convection, saturated boiling, nucleate boiling and film evaporation. For both 100 and 150 ml/min tests, film evaporation during annular flow was the best mechanisms for heat removal. However, due to the unstable scheme in annular flow for the 200 ml/min test, the nucleation boiling during plug flow was observed as the best cooling scenario.

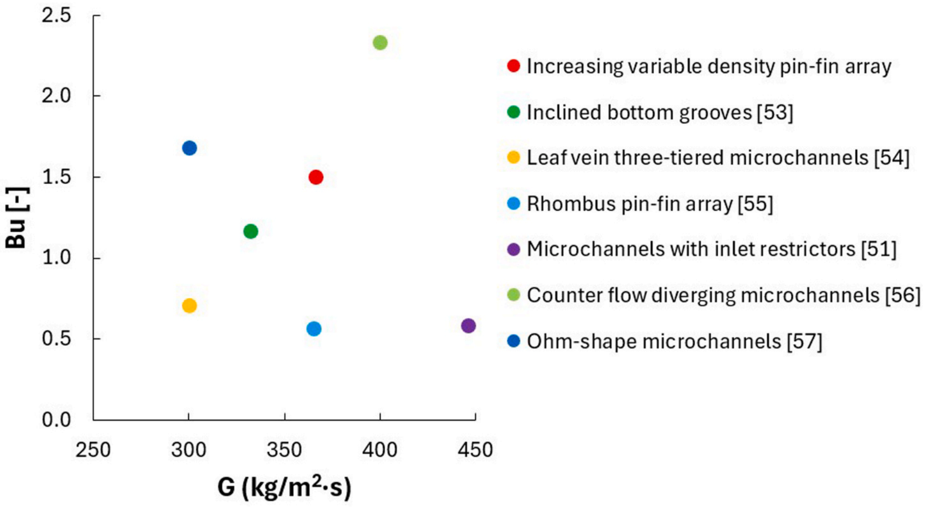

Fig. 20. Boiling utilization comparison map.

- From a quantitative point of view, for the 100, 150 and 200 ml/min tests, the ONB occurred at 2.46, 3.29 and 6.20 °C of wall temperature and the CHF occurred at 32.31, 40.31 and 58.11 W/cm^2, respectively. The maximum thermal heat transfer coefficients were 5929, 7173 and 9323 $W/°C{\cdot}m^2$. In comparison with their initial stages of bubbly flow, the achieved enhancement was of 33.96, 64.95 and a 51.02 %, respectively.
- UCVI and its consequent reversal flow were the most problematic instabilities, leading to a boiling crisis when heat flux increase. A flow instability map was plotted to give an overview of the heatsink performance.
- The dimensionless parameter Boiling Utilization (Bu) was used to evaluate and compare the flow boiling performance of the proposed cooling device with similar works from the literature. Results indicate that the increasing variable pin-finned surface design is a promising solution, though it requires further development.

The results of this study may help researchers and designers to orient their flow boiling cooling solutions in pin-fins devices. However, numerical and experimental research is still needed to identify general guidelines that can facilitate finding one or more optimal designs.

Declaration of competing interest

The authors declare the following financial interests/personal relationships which may be considered as potential competing interests: Manel Ibanez reports financial support was provided by Spain Ministry of Science and Innovation. Jaume Camarasa reports financial support was provided by University of Lleida. If there are other authors, they declare that they have no known competing financial interests or personal relationships that could have appeared to influence the work reported in this paper.

Acknowledgment

This work is part of R+D+I Project PID2021-123634OB-I00, funded by MCIN / AEI/ 10.13039/501100011033.

Jaume Camarasa would like to thank Universitat de Lleida for supporting his research by “Ajut UdL per a la contractació de personal predoctoral en formació (2023-2026)”.

The authors would like to thank Generalitat de Catalunya for the project awarded to their research group Sustainability in Energy, Machinery and Buildings (2021 SGR 01370).

Data availability

Data will be made available on request.

References

[1] D.B. Tuckerman, R.F.W. Pease, High-Performance Heat Sinking for VLSI, 1981.
[2] G. Liang, I. Mudawar, Review of pool boiling enhancement by surface modification, (Jan. 01, 2019) Elsevier Ltd. doi: 10.1016/j.ijheatmasstransfer.2018.09.026.
[3] I. Mudawar, Two-phase microchannel heat sinks: theory, applications, and limitations, J. Electron. Packag. Trans. ASME 133 (4) (2011), https://doi.org/10.1115/1.4005300.
[4] B. Parizad Benam, A. Khalili Sadaghiani, V. Ya, M. Parlak, K. Sefiane, A. Ko, Review on high heat flux flow boiling of refrigerants and water for electronics cooling, Int. J. Heat Mass Transf. 180 (2021) 121787, https://doi.org/10.1016/j.ijheatmasstransfer.2021.121787.
[5] G. Liang, I. Mudawar, Review of channel flow boiling enhancement by surface modification, and instability suppression schemes, Int. J. Heat Mass Transf. 146 (2020) 118864, https://doi.org/10.1016/j.ijheatmasstransfer.2019.118864.
[6] D. Deng, L. Zeng, W. Sun, A review on flow boiling enhancement and fabrication of enhanced microchannels of microchannel heat sinks, Int. J. Heat Mass Transf. 175 (2021) 121332, https://doi.org/10.1016/j.ijheatmasstransfer.2021.121332.
[7] J. Camarasa, A. Crespo, M. Vilarrubí, M. Ibáñez, J. Barrau, A review of experimental studies on flow boiling instabilities mitigation through geometrical modifications, Int. J. Heat Mass Transf. 235 (Dec. 2024) 126014, https://doi.org/10.1016/j.ijheatmasstransfer.2024.126014.
[8] G. Hetsroni, A. Mosyak, E. Pogrebnyak, Z. Segal, Explosive boiling of water in parallel micro-channels, Int. J. Multiph. Flow 31 (2005) 371–392, https://doi.org/10.1016/j.ijmultiphaseflow.2005.01.003.
[9] H.Y. Wu, P. Cheng, Boiling instability in parallel silicon microchannels at different heat flux, Int. J. Heat Mass Transf. 47 (2004) 3631–3641, https://doi.org/10.1016/j.ijheatmasstransfer.2004.04.012.
[10] D. Deng, Y. Xie, Q. Huang, Y. Tang, L. Huang, X. Huang, Flow boiling performance of Ω-shaped reentrant copper microchannels with different channel sizes, Exp. Therm. Fluid Sci. 69 (Dec. 2015) 8–18, https://doi.org/10.1016/j.expthermflusci.2015.07.016.
[11] Y. Lan, et al., Experimental investigation on the effects of swirling flow on flow boiling heat transfer and instability in a minichannel heat sink, Appl. Therm. Eng. 219 (2022), https://doi.org/10.1016/j.applthermaleng.2022.119512.
[12] D. Deng, L. Chen, X. Chen, G. Pi, Heat transfer and pressure drop of a periodic expanded-constrained microchannels heat sink, Int. J. Heat Mass Transf. 140 (2019) 678–690, https://doi.org/10.1016/j.ijheatmasstransfer.2019.06.006.
[13] D.D. Ma, Y.X. Tang, G.D. Xia, Experimental investigation of flow boiling performance in sinusoidal wavy microchannels with secondary channels, Appl. Therm. Eng. 199 (2021), https://doi.org/10.1016/j.applthermaleng.2021.117502.
[14] D. Wang, D. Wang, F. Hong, C. Zhang, J. Xu, Improved flow boiling performance and temperature uniformity in counter-flow interconnected microchannel heat sink, Appl. Therm. Eng. 241 (Mar. 2024), https://doi.org/10.1016/j.applthermaleng.2024.122370.
[15] K. Ren, W. Yuan, Z. Miao, B. Yang, Influence of inlet/outlet arrangement on flow boiling of a parallel strip fin heat sink, Appl. Therm. Eng. 176 (Jul. 2020), https://doi.org/10.1016/j.applthermaleng.2020.115061.
[16] Y. Li, H. Wu, Y. Yao, Enhanced flow boiling heat transfer and suppressed boiling instability in counter-flow stepped microchannels, Int. J. Heat Mass Transf. 194 (2022) 123025, https://doi.org/10.1016/j.ijheatmasstransfer.2022.123025.
[17] S. Szczukiewicz, N. Borhani, J.R. Thome, Two-phase flow operational maps for multi-microchannel evaporators, Int. J. Heat Fluid Flow 42 (2013) 176–189, https://doi.org/10.1016/j.ijheatfluidflow.2013.03.006.
[18] A. Koşar, C.J. Kuo, Y. Peles, Boiling heat transfer in rectangular microchannels with reentrant cavities, Int. J. Heat Mass Transf. 48 (23–24) (Nov. 2005) 4867–4886, https://doi.org/10.1016/j.ijheatmasstransfer.2005.06.003.
[19] C.J. Kuo, Y. Peles, Pressure effects on flow boiling instabilities in parallel microchannels, Int. J. Heat Mass Transf. 52 (1–2) (Jan. 2009) 271–280, https://doi.org/10.1016/j.ijheatmasstransfer.2008.06.015.
[20] A. Kalani, S.G. Kandlikar, Evaluation of pressure drop performance during enhanced flow boiling in open microchannels with tapered manifolds, J. Heat Transfer 136 (5) (May 2014), https://doi.org/10.1115/1.4026306.
[21] W. Li, et al., Supercapillary architecture-activated two-phase boundary layer structures for highly stable and efficient flow boiling heat transfer, Adv. Mater. 32 (2) (Jan 2020), https://doi.org/10.1002/adma.201905117.
[22] J. Zhou, X. Chen, Q. Zhao, M. Lu, D. Hu, Q. Li, Flow thermohydraulic characterization of hierarchical-manifold microchannel heat sink with uniform flow distribution, Appl. Therm. Eng. 198 (2021), https://doi.org/10.1016/j.applthermaleng.2021.117510.
[23] A. Priy, S. Raj, M. Pathak, M. Kaleem Khan, A hydrophobic porous substrate-based vapor venting technique for mitigating flow boiling instabilities in microchannel heat sink, Appl. Therm. Eng. 216 (2022), https://doi.org/10.1016/j.applthermaleng.2022.119138.
[24] Z. Zhang, Y. Wu, K. He, X. Yan, Experimental investigation into flow boiling heat transfer and pressure drop in porous coated microchannels, Int. J. Heat Mass Transf. 218 (Jan. 2024), https://doi.org/10.1016/j.ijheatmasstransfer.2023.124734.
[25] C.S. Sujith Kumar, S. Suresh, C.R. Aneesh, M.C. Santhosh Kumar, A.S. Praveen, K. Raji, Flow boiling heat transfer enhancement on copper surface using Fe doped Al2O3 -TiO2 composite coatings, Appl. Surf. Sci. 334 (Apr. 2015) 102–109, https://doi.org/10.1016/j.apsusc.2014.08.076.
[26] A.S. Kousalya, K.P. Singh, T.S. Fisher, Heterogeneous wetting surfaces with graphitic petal-decorated carbon nanotubes for enhanced flow boiling, Int. J. Heat Mass Transf. 87 (Aug. 2015) 380–389, https://doi.org/10.1016/j.ijheatmasstransfer.2015.04.029.
[27] I. Pranoto, K.C. Leong, An experimental study of flow boiling heat transfer from porous foam structures in a channel, Appl. Therm. Eng. 70 (2014) 100–114, https://doi.org/10.1016/j.applthermaleng.2014.04.027.
[28] Q. Zhao, J. Qiu, J. Zhou, M. Lu, Q. Li, X. Chen, Visualization study of flow boiling characteristics in open microchannels with different wettability, Int. J. Heat Mass Transf. 180 (2021) 121808, https://doi.org/10.1016/j.ijheatmasstransfer.2021.121808.
[29] V.E. Ahmadi, et al., Effect of mixed wettability surfaces on flow boiling heat transfer at subatmospheric pressures, Appl. Therm. Eng. 236 (Jan. 2024), https://doi.org/10.1016/j.applthermaleng.2023.121476.
[30] D.P. Ghosh, D. Sharma, A. Kumar, S. Kumar Saha, R. Raj, An ingenious fluidic capacitor for complete suppression of thermal fluctuations in two-phase microchannel heat sinks, Int. Commun. Heat Mass Transf. 110 (2019), https://doi.org/10.1016/j.icheatmasstransfer.2019.104347.
[31] G. Hedau, R. Raj, S.K. Saha, Complete suppression of flow boing instability in microchannel heat sinks using a combination of inlet restrictor and flexible dampener, Int. J. Heat Mass Transf. 182 (2022) 121937, https://doi.org/10.1016/j.ijheatmasstransfer.2021.121937.
[32] A. Mohammadi, A. Koşar, in: Review on Heat and Fluid Flow in Micro Pin Fin Heat Sinks under Single-phase and Two-phase Flow Conditions, Taylor and Francis Inc., Jul. 03 2018, https://doi.org/10.1080/15567265.2018.1475525.

[33] D. Deng, L. Zeng, W. Sun, G. Pi, Y. Yang, Experimental study of flow boiling performance of open-ring pin fin microchannels, Int. J. Heat Mass Transf. 167 (2021) 120829, https://doi.org/10.1016/j.ijheatmasstransfer.2020.120829.

[34] L.-H. Chien, W.-R. Liao, M. Ghalambaz, W.-M. Yan, Experimental study on convective boiling flow and heat transfer in a microgap enhanced with a staggered arrangement of nucleated micro-pin-fins, Int. J. Heat Mass Transf. 144 (2019), https://doi.org/10.1016/j.ijheatmasstransfer.2019.118653.

[35] C. Woodcock, X. Yu, J. Plawsky, Y. Peles, Piranha Pin Fin (PPF)-Advanced flow boiling microstructures with low surface tension dielectric fluids, Int. J. Heat Mass Transf. 90 (2015) 591–604, https://doi.org/10.1016/j.ijheatmasstransfer.2015.06.072.

[36] X. Ma, X. Ji, J. Wang, J. Fang, Y. Zhang, J. Wei, Flow boiling heat transfer characteristics on micro-pin-finned surfaces in a horizontal narrow microchannel, Int. J. Heat Mass Transf. 194 (2022) 123071, https://doi.org/10.1016/j.ijheatmasstransfer.2022.123071.

[37] M. Law, P.-S. Lee, Effects of varying secondary channel widths on flow boiling heat transfer and pressure characteristics in oblique-finned microchannels, Int. J. Heat Mass Transf. 101 (2016) 313–326, https://doi.org/10.1016/j.ijheatmasstransfer.2016.05.055.

[38] B. Markal, A. Evcimen, F. Atci, O. Aydin, Investigation of heat transfer limits for flow boiling in expanding heat sinks having micro pin fins, Int. Commun. Heat Mass Transf. 156 (Aug. 2024), https://doi.org/10.1016/j.icheatmasstransfer.2024.107650.

[39] B. Markal, B. Kul, M. Avci, R. Varol, Effect of gradually expanding flow passages on flow boiling of micro pin fin heat sinks, Int. J. Heat Mass Transf. 197 (2022), https://doi.org/10.1016/j.ijheatmasstransfer.2022.123355.

[40] B. Markal, B. Kul, Influence of downstream cross-sectional area ratio on flow boiling characteristics of expanding micro pin fin heat sinks, Int. Commun. Heat Mass Transf. 143 (2023) 106689, https://doi.org/10.1016/j.icheatmasstransfer.2023.106689.

[41] J. Barrau, S. Riera, E. Léveillé, L.G. Fréchette, J.I. Rosell, Nozzle to plate optimization of the jet impingement inlet of a tailored-width microchannel heat exchanger, Exp. Therm Fluid Sci. 67 (Oct. 2015) 81–87, https://doi.org/10.1016/j.expthermflusci.2014.11.012.

[42] S. Riera, J. Barrau, M. Omri, L.G. Fréchette, J.I. Rosell, Stepwise varying width microchannel cooling device for uniform wall temperature: Experimental and numerical study, Appl. Therm. Eng. 78 (Mar. 2015) 30–38, https://doi.org/10.1016/j.applthermaleng.2014.12.012.

[43] M. Vilarrubí, et al., Experimental and numerical study of micro-pin-fin heat sinks with variable density for increased temperature uniformity, Int. J. Therm. Sci. 132 (Oct. 2018) 424–434, https://doi.org/10.1016/j.ijthermalsci.2018.06.019.

[44] S.J. Kline, F.A. McClintock, Describing uncertainties in single-sample experiments, Mech. Eng. 75 (1953) 3–8.

[45] Y. Hui, X. Li, R. Lei, H. Hu, Boiling heat transfer characteristics of distributed jet array impingement on metal foam covers with different wettability, Int. J. Refrig. 167 (Nov. 2024) 90–101, https://doi.org/10.1016/j.ijrefrig.2024.08.001.

[46] B. He, et al., Effects of inlet subcooling on the flow boiling heat transfer performance of bi-porous mini-channels, Appl. Therm. Eng. 229 (2023) 120577, https://doi.org/10.1016/j.applthermaleng.2023.120577.

[47] A. Ateş, et al., On the effect of elliptical pin Fins, distribution pin Fins, and tip clearance on the performance of heat sinks in flow boiling, Appl. Therm. Eng. 212 (Jul. 2022), https://doi.org/10.1016/j.applthermaleng.2022.118648.

[48] A. Ateş, V. Yağcı, M.Ç. Malyemez, M. Parlak, A. Sadaghiani, A. Koşar, Flow dynamics characteristics of flow boiling in minichannels with distributed pin fin structures, Int. J. Therm. Sci. 199 (May 2024), https://doi.org/10.1016/j.ijthermalsci.2024.108912.

[49] Q. Zhao, et al., Irregular-shaped nucleated bubbles induced enhancement of subcooled flow boiling heat transfer in leaf vein inspired three-tiered open microchannels (LTOMCs), Int. J. Heat Mass Transf. 211 (2023) 124281, https://doi.org/10.1016/j.ijheatmasstransfer.2023.124281.

[50] L. Yin, Y. Wang, L. Jia, Flow boiling instability of R134a in the large-area heat sink with interconnected parallel multi-minichannels, Int. J. Therm. Sci. 204 (Oct. 2024), https://doi.org/10.1016/j.ijthermalsci.2024.109193.

[51] X. Cheng, H. Wu, Impact of inlet subcooling on flow boiling in microchannels, Exp. Therm. Fluid Sci. 142 (2023) 110805, https://doi.org/10.1016/j.expthermflusci.2022.110805.

[52] X. Cheng, et al., Deionized water flow boiling in low-surface-roughness silicon-based high aspect ratio interconnected microchannels, Int. J. Heat Mass Transf. 238 (Mar. 2025), https://doi.org/10.1016/j.ijheatmasstransfer.2024.126454.

[53] Y. Bian, et al., Experimental investigation on the effects of inclined grooves on flow boiling heat transfer and instability in a minichannel heat sink, Int. J. Heat Mass Transf. 236 (Jan. 2025) 126333, https://doi.org/10.1016/j.ijheatmasstransfer.2024.126333.

[54] Q. Zhao, J. Zhou, M. Lu, X. Chen, Multi-tiered configurations improved flow boiling performance: Comparation investigation of leaf vein inspired two-tiered and three-tiered open microchannels, Int. J. Therm. Sci. 201 (Jul. 2024), https://doi.org/10.1016/j.ijthermalsci.2024.109021.

[55] Q. Zhao, M. Lu, J. Zhou, Y. Zhang, Q. Li, X. Chen, A high-fidelity sharkskin inspired placoid-scales structured microchannel (SPMC) for advancement of heat transfer performance, Int. J. Heat Mass Transf. 224 (Jun. 2024), https://doi.org/10.1016/j.ijheatmasstransfer.2024.125301.

[56] X. Jiang, S. Zhang, Y. Li, C. Pan, High performance heat sink with counter flow diverging microchannels, Int. J. Heat Mass Transf. 162 (2020) 120344, https://doi.org/10.1016/j.ijheatmasstransfer.2020.120344.

[57] D. Deng, W. Wan, Y. Tang, Z. Wan, D. Liang, Experimental investigations on flow boiling performance of reentrant and rectangular microchannels-A comparative study, Int. J. Heat Mass Transf. 82 (2014) 435–446, https://doi.org/10.1016/j.ijheatmasstransfer.2014.11.074.